2. Experimental Details

In the following chapter, the details of the experimental setup will be introduced. The setup essentially consists in an ultra-high vacuum chamber and an amplified fs-laser system delivering 800-nm laser pulses. For the time-resolved investigations via sum-frequency generation (SFG) the 800-nm pulses are converted into infrared (IR) pulses, whereas for the state-resolved experiments via resonance enhanced multi photon ionization (REMPI) the setup is combined with a tunable dye-laser system. After a brief description of the vacuum and laser systems, the applied experimental methods are explained. The chapter ends with a final section sketching the technical implementation of the experiments.

2.1. Vacuum system

For the understanding of the investigated surface reactions it is essential to work with well defined surfaces. An ultra-high vacuum (UHV) surrounding is required, so that adsorption of gas particles onto the surface under investigation can be neglected for the duration of the experiment. The pressure range providing this condition is $\leq 1 \cdot 10^{-10}$ mbar and is realized in the experiment by pumping a stainless steel UHV chamber with the combination of two turbomolecular pumps and a membrane pump. The UHV chamber is baked out after each venting [Yat98] in order to speed up the achievement of the UHV regime by removing adsorbed impurities (most likely water) from the chamber wall. The composition of the residual gas is determined with a mass spectrometer and shown in Fig. 2.1 where not only intact molecules (mainly H_2, H_2O, CO and CO_2) are detected but also their fragments (H, O and OH) due to cracking of the molecular bond during ionization. The overall pressure is measured with a Bayard-Alpert ionization pressure gauge, applicable in the pressure range from 10^{-4} to $5 \cdot 10^{-11}$ mbar.

2.1.1. Sample mounting, heating, cooling and positioning

The preparation of the desired adsorbate structures requires the control of the surface temperature and the possibility to offer gases in a defined manner to the sample surface. Therefore as shown in Fig. 2.2, the Ru(001) crystal is mounted electrically isolated to a continuous flow cryostat for cooling, which together with two different types of heating allow to access a sample-temperature range from 20 to 1530 K. The temperature is measured with a type K thermocouple spot-welded to the side of the crystal. The cryostat works either with liquid nitrogen or liquid helium, and its temperature is controlled via an internal heating and a temperature sensor. The heating of the Ru(001) crystal can either be realized by a resistive heating, where a current of maximum 22 A heats the thin Ta wires holding the crystal, or by electron bombardment, whereby electrons from a filament are accelerated towards the

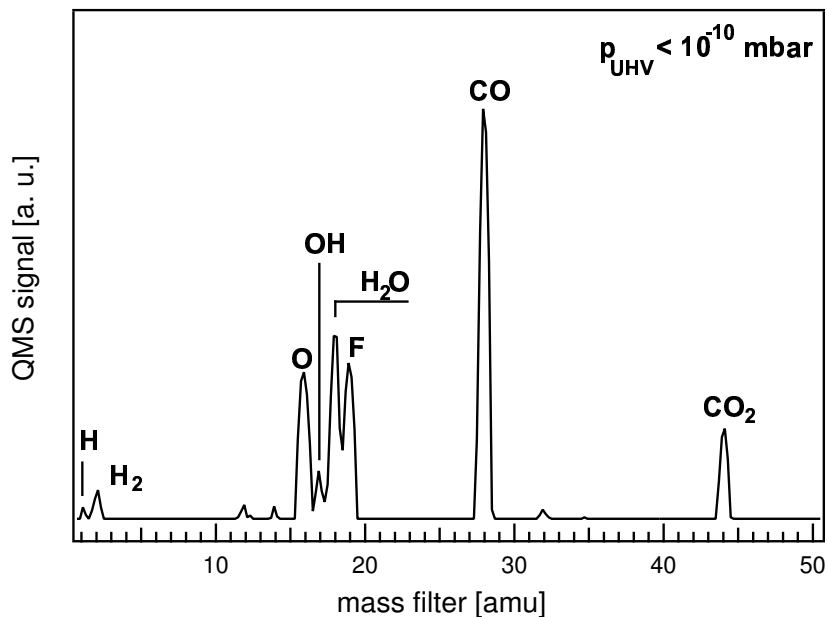**Figure 2.1.:** Residual gas spectrum at a chamber pressure $\leq 1 \cdot 10^{-10}$ mbar mainly consisting of H_2, H_2O, CO and CO_2 features. The signal at mass 19 is an artefact resulting from the electron-stimulated desorption of flourine in the rod system of the QMS.

backside of the sample. A typical emission current of 20 mA with a negative bias of 1 kV on the filament allows heating of the crystal to temperatures as high as 1530K, whereas with the resistive heating no temperatures higher than 850K are achievable. Therefore, the electron bombardment heating is mainly applied in crystal cleaning procedures (Section 2.1.2), whereas resistive heating is used for controlling the sample temperature and temperature programmed desorption (TPD) experiments (Section 2.4.1).

The cryostat is mounted to a stepping motor controlled XYZ manipulator which in combination with a differentially pumped rotational stage allows to move the sample in all directions in space and rotate it towards the required direction. Figure 2.3 shows the two different UHV chambers used in the different experiments. The optical paths for the performed experiments (see Section 2.5.1 and Section 2.5.2) are shown, as well as the position of the applied instruments. For both chambers additional leak valves are mounted, which allow to set a desired background pressure of any gas. For a more defined gas exposure to the sample a pinhole doser can be used. The eponymous pinhole consists of a $5\,\mu$m aperture which separates the UHV from a gas reservoir. The therein contained gas streams through the pinhole and is guided by a stainless steel tube directly to the Ru(001) surface so that gas dosing is possible with a minimum of chamber wall reactions and gas load to the vacuum. Leak valves and pinhole doser are connected to a gas system, where bottles of the required gases (H_2, D_2, Ar, O_2, CO and C_2H_4) are connected and the pressure in the gas reservoir leading to the pinhole doser can be controlled. For a more detailed description see [Fun99].

The sputter gun is used in crystal cleaning procedures (see Section 2.1.2) and the various quadrupole mass spectrometers (QMS) are either applied for time-of-flight (TOF) measurements in laser induced desorption experiments or for temperature-programmed desorption (TPD) (see Section 2.5). For the latter purpose, one of the QMSs inside the "SFG" chamber
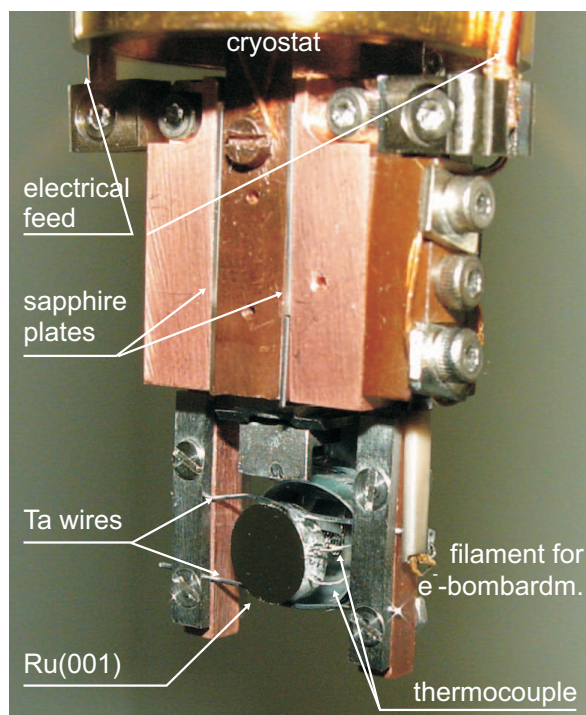
Figure 2.2.: Photograph of the sample holder. It consists of an electrically grounded center part mounted to a continuous flow cryostat, which can be cooled either with liquid helium or liquid nitrogen. The two outer parts of the sample holder are electrically isolated by sapphire plates in-between the copper blocks. The Ru(001) single crystal is held by two Ta wires ($\varnothing$ 0.4 mm) which are clamped to the outer copper blocks. An electrical feed connection on each of these copper blocks allows sending an electrical current through the Ta wires, which heat up and thereby also the crystal. Behind the crystal an electrically isolated filament is visible wherefrom electrons are accelerated to the crystal for electron bombardment heating. A sample temperature of ≈ 20 to 1530 K can be set and is measured with a type K thermocouple spot-welded to the side of the crystal.

is equipped with a so-called "Feulner"-Cup [Feu80], which allows to measure the desorption from the sample's surface almost background free and angle-integrated, which is not possible with a non-shielded QMS. For technical details, convincing examples and etymology see [Den03a, Yat98, Feu80]. The other mass spectrometers are mounted in line-of-sight to the samples surface so that it is possible to measure the desorbates'[1] time-of-flight distribution with the QMS. Since the flight time from the surface to the ionizer of the QMS is the shorter the smaller the mass of the desorbing species is[2], the non-shielded QMS in the upper level of the "SFG"-chamber is mounted to an moveable extension flange, so that the measured H_2/D_2 TOF spectra for the very fast molecules are spread in time (see Section 2.5.1) and a better temporal resolution is obtained.

Regarding the "REMPI" chamber, a multi-channel plate (MCP) ion detector is mounted at a lower (not shown) chamber level. Its front side points upwards, towards the sample holder. The flight time of the ions from the location of formation (Section 2.5.1) to the detector can be varied by biasing a grid in front of the detector with an adjustable high voltage. The amplification of the ion signal is achieved by two MCPs, each of them connected to an

---

[1]Please concede me the freedom to expand the English language with this notion that is equally reasoned as its time-reversed cousin, the adsorbate.
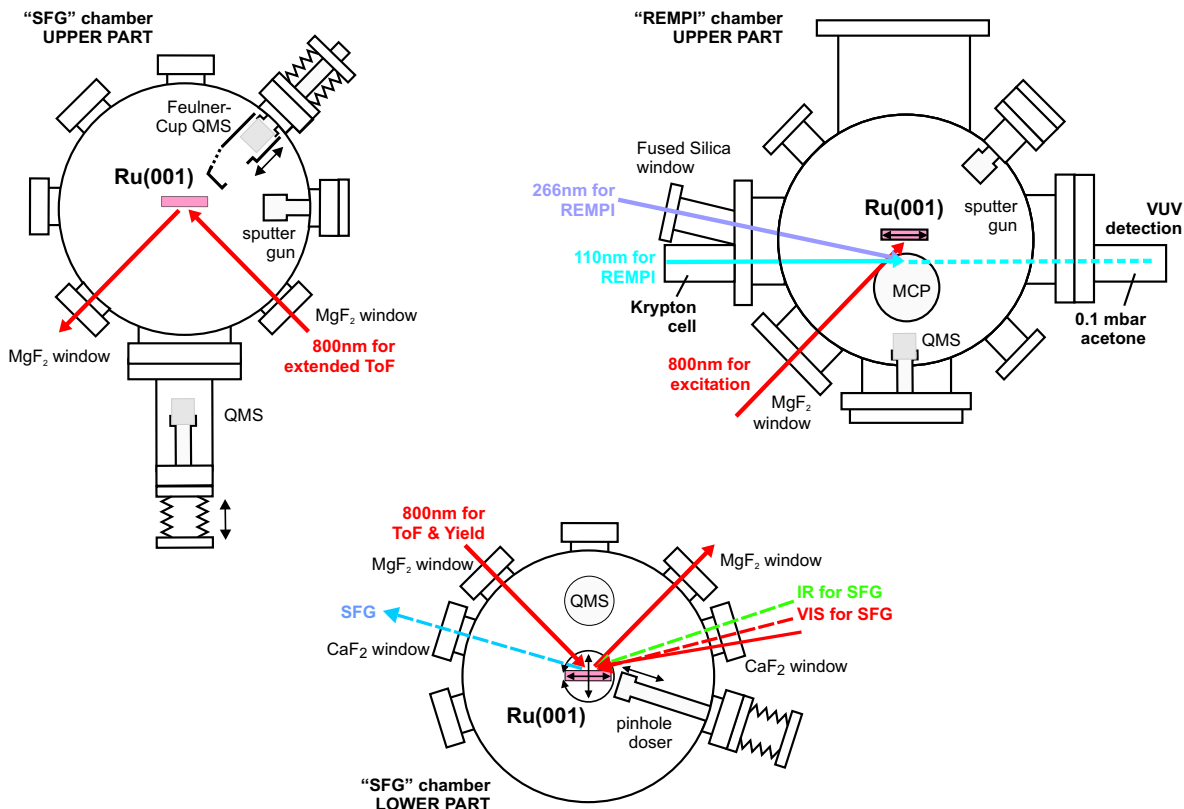
[2]assuming same kinetic energy

Figure 2.3.: Illustration of the two UHV chambers that are used in the present experiments. The left and the bottom two levels of the "SFG"-chamber are shown, whereas on the right the "REMPI"-chamber is depicted. The chambers are named after the experiments mainly applied with them. In addition, the positions are shown and the applied laser pulses are indicated by arrows.

amplification voltage of 1 kV. The obtained signal strength is in the order of 1 to 10 mV. Details of the optical components mounted to the "REMPI"-chamber and the performance of the experiment can be found in Section 2.3 and Section 2.5.1.

2.1.2. Preparation of the Ru(001) surface

As already mentioned, well-defined, atomically ordered surfaces are essential for the understanding of the investigated surface reactions. Therefore, the preparation and characterization of the Ru(001) single crystal surface is described and the differences between an initial and a daily preparation procedure are discussed.

Initial preparation

The Ru(001) single crystal (thickness 2 mm, $\varnothing$ 8 mm) is cut from a single crystal rod with an orientation accuracy $\leq 0.5°$ and afterwards polished. Remaining impurities from the grinding paste and intrinsic impurities, mostly carbon, oxygen and sulphur [Mus82], are removed by repeated heating and sputtering. The sputtering has been carried out at a crystal temperature of 1000 K and an Ar pressure of $2 \cdot 10^{-5}$ mbar with a cycle time of 20 minutes. The Ar^+ ions

were accelerated to $3\,\mathrm{kV}$, and the sample was moved continuously in a plane perpendicular to the ion beam to assure that the surface is sputtered homogeneously. The subsequent heating was performed with an O_2 pressure of $2 \cdot 10^{-7}$ mbar and a crystal temperature of 1500 K for another 20 minutes. Whereas in the sputtering step surface atoms are ablated and the surface is roughened, the heating heals up the surface and impurities diffuse to surface, oxidize and desorb, and an impurity-poor surface region is obtained.

The surface quality is checked with thermal desorption spectra (TDS), since they react very sensitive to impurities [Den03a, Fun99]. The absence of carbon is verified if no CO desorption occurs in the temperature range of from 400 to 1100 K after having saturated the surface with oxygen at room temperature. The most precise information about the surface quality is obtained by adsorption of molecular CO and subsequent thermal desorption. The shape of the desorption maxima in the TD spectra are very sensitive to impurities [Kos92, Pfn83] and thus suited to judge the surface quality even quantitatively.

Daily preparation

The daily preparation procedure is similar to above mentioned initial one, but differs with respect of sputter energies and annealing times. The applied sputter parameters are $2 \cdot 10^{-5}$ mbar Ar pressure, $0.5\,\mathrm{kV}$ acceleration voltage and 20 minutes duration. This leads to an ion current of 5 μA onto the sample. The subsequent annealing in $2 \cdot 10^{-7}$ mbar O_2 atmosphere is carried out for 5 minutes at a crystal temperature of $1250\,\mathrm{K}$. The adsorbed oxygen is desorbed by heating the sample several times for $10\,\mathrm{seconds}$ to $1530\,\mathrm{K}$. The surface quality is again checked by a CO TDS, as shown in Section 4.1.2.

2.2. Femtosecond-laser system

The present thesis is based on the investigation of surface reactions induced by ultrashort, i.e. femtosecond (fs) laser pulses. For the investigation of the associative H_2/D_2 desorption (Section 2.5.1) the ultrashort laser pulse was "only" used to induce the reaction, whereas for the CO recombination (Section 2.5.2) the pulse was in addition frequency converted to an infrared (IR) pulse and applied for time-resolved vibrational spectroscopy to monitor the intramolecular CO stretch vibration. Therefore, after a brief description of the generation and amplification of the ultrashort laser pulses, the generation of an ultrashort infrared (IR) pulse is discussed as well.

2.2.1. Femtosecond-laser pulse generation and amplification

The generation of the intense ultrashort laser pulses used in the experiments described in this thesis is based on a Ti:Sapphire (Ti:Sa) fs-oscillator and a two-stage amplifier system. Figure 2.4 shows the schematic setup, which delivers pulses of $\approx 100\,\text{fs}$ duration, $800\,\text{nm}$ central frequency and up to $4.0\,\text{mJ}$ and a repetition rate manually adjustable from 10 to $400\,\text{Hz}$.
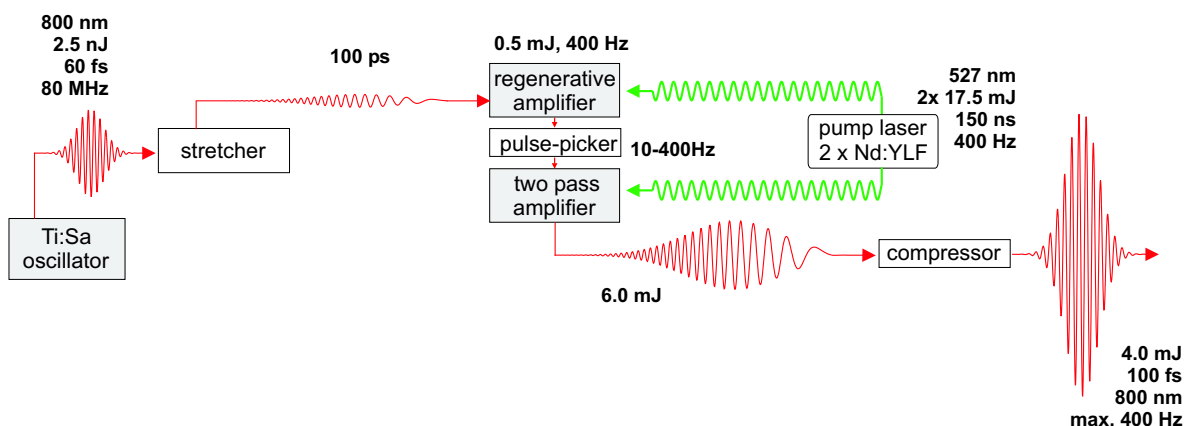

Figure 2.4.: Schematic diagram of the laser system. The fs oscillator delivers low energy pulses at a high repetition rate, which are stretched in time first amplified regeneratively. After a second amplifier stage (2 pass), the pulses are compressed in time. Typical pulse characteristics are given.

The laser medium Ti:Sa, which shows a broad vibronic fluorescence band, allows light amplification from 670 to $1070\,\text{nm}$ with the peak of the gain curve around $800\,\text{nm}$ [Koe96]. Ti:Sa also has a broad absorption band with maximum absorption around $500\,\text{nm}$, which is well separated from the fluorescence band and allows pumping the laser medium with a frequency doubled Nd:YLF laser, delivering $150\,\text{ns}$ pulses at $527\,\text{nm}$.

Generation of fs-pulses

The minimum pulse width obtainable from a Q-switched laser is in the order of $10\,\text{ns}$. Ultrashort pulses with pulse widths in the femtosecond regime are nowadays obtained from solid-state lasers by mode-locking, where one utilizes the coherence of the laser process. In a free-running *cw* laser, all possible resonator modes oscillate without fixed mode-to-mode
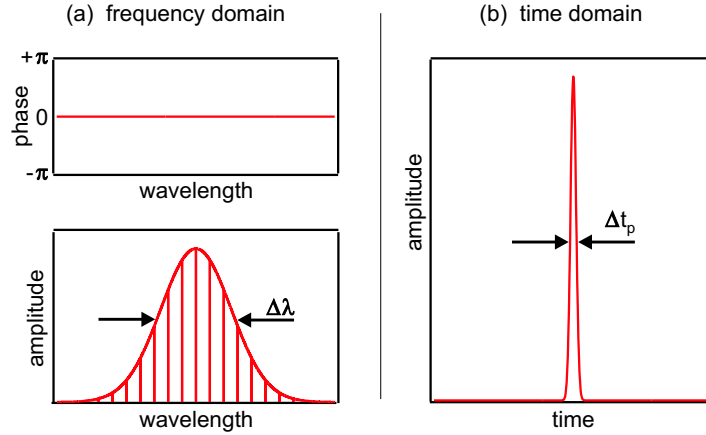
Figure 2.5.: Signal structure of an ideally mode-locked laser. The spectral intensities (a) have a Gaussian distribution, while the spectral phases are identically zero. In the time domain (b) the signal is a transform-limited Gaussian pulse. (Figure taken from [Den03a].)

phase relations. If in contrast the modes are forced to maintain fixed phase relations to each other, the temporal output of the sub ns-range. The laser is then said to be "mode-locked" and the output signal is well defined as shown in Fig. 2.5.

The generation of mode-locked pulses is achieved experimentally either by placing an externally driven loss or phase modulator inside the laser cavity (active mode-locking), or a passive device which exhibits saturable absorption. In the oscillator used in the present experiment, the mode-locking is achieved by the combination of the optical Kerr-effect and an aperture introduced to the laser resonator. The optical Kerr-effect is a variation of the refractive index $n(\omega, I)$ of a material due to the electric field of the light itself and is given by

$$n(\omega, I) = n_0(\omega) + n_2 \, I(\omega, t). \tag{2.1}$$

This change in the index of refraction only becomes significant with high beam intensities I. For a Gaussian beam, the Kerr effect focuses the radiation towards the center, essentially an intensity-dependent graded-index lens is formed. The transformation of the power-dependent change in the spatial profile of the beam into an amplitude modulation is illustrated in Figure 2.6. The weak parts of the beam are either suppressed by an aperture (Figure 2.6a shows the so-called "hard aperture mode locking") or less amplified due to worse overlap with the pump beam (Figure 2.6b sketches "soft aperture mode locking"). This leads to mode-locking and thus to a shortening of the pulse[3] with each resonator round trip, until an equilibrium between pulse shortening, dispersive pulse broadening and gain narrowing[4] is established.

The two oscillators mainly used in the presented experiments are both Kerr lens mode-locked. The Coherent-Mira-fs-oscillator works with the "hard aperture mode-locking"-principle and delivers laser pulses of 95 fs duration, a spectral full width at half maximum (FWHM) of 12 nm and pulse energies of 12 nJ at a repetition rate of 76 MHZ. Its replacement, a Coherent-Vitesse-Seed oscillator based on the "soft aperture mode-locking"-principle works at a repetition rate of 80 MHz and generates pulses of 60 fs duration, 35 nm spectral width (FWHM) and 2.5 nJ pulse energy.

---

[3]In the frequency domain, extra phase-locked modes are generated because of self-phase modulation.
[4]The bandwidth of light can be reduced during amplification in a medium with limited gain bandwidth.

(a) hard aperture mode locking
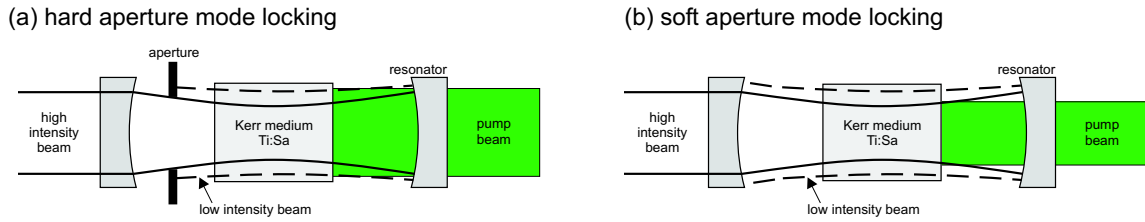
(b) soft aperture mode locking

Figure 2.6.: Kerr lens mode-locking: intensity dependent amplitude modulation of the resonator mode. The self-focusing of the high intensity beam reduces the optical losses at the aperture (a) or leads to a better overlap of laser and pump beam (b).

Amplification of fs-pulses

The energy of the laser pulses generated by the femtosecond oscillator is not sufficient for the experiments presented here. Therefore the pulses have to gain energy outside the oscillator in additional amplification stages. The chirped-pulse amplification (CPA) technique was developed to reduce the enormous peak powers in these amplifiers, which would otherwise limit the output energy because of intensity-dependent pulse distortions and damage of the amplifier components. In this technique, strongly dispersive elements are used to expand the pulse width at the entrance to the amplifier system by several orders of magnitude and thereby reduces peak powers. After the gain medium, a dispersive compressor which removes the chirp and temporally compresses the pulses to a duration similar to the input pulse duration. In our setup, gratings are used for the stretching and compressing process.

The stretched pulse is coupled into the regenerative amplifier by an optical switch, which is realized by the combination of a thin film polarizer (TFP) and a Pockels cell[5]. This Pockels cell is operated at a frequency of $400\,\text{Hz}$ and synchronized to the repetition rate of the Nd:YLF pump laser. One pulse remains for ≈ 18 round trips in the RGA resonator, while it is continuously amplified, and is then coupled out when amplification saturation is reached. Between the RGA and the final amplification, a pulse picker is set up. This pulse picker is realized by a second Pockels cell in-between two crossed polarizers. It is required for the suppression of unwanted possible pre- and post-pulses out of the RGA and additionally offers the possibility of decreasing the repetition rate further down to a minimum of 10 Hz. The final amplification is performed by passing the pulse twice through another Ti:Sa crystal which is also synchronously pumped by two Nd:YLF lasers. Finally the pulse is compressed to a pulse length of $\sim 100\,\text{fs}$, where the reflections on the grating cause an energy loss of $\sim 35\%$.

The main characteristics of the laser pulses at each stage of the amplification process are given in Fig. 2.4 (p. 36). A more detailed description of the fs laser system can be found in [Fun99].

2.2.2. Femtosecond-IR pulses generation

The ultrashort IR laser pulses are generated by an optical parametric amplifier (OPA), which is pumped by the fs-laser system described in the previous section. The OPA is based on a

---

[5]A Pockels cell is a device consisting of an electro-optic crystal through which the light propagates. By applying a high voltage one can modulate the phase delay in the birefringent crystal, so that one has a voltage-controlled waveplate.

special case of 3-wave mixing, in which an incident laser pulse with frequency ω_3 is divided by a non-linear optical crystal into two beams with frequencies ω_1 and ω_2 fulfilling the energy conservation $\omega_3 = \omega_1 + \omega_2$. The generated light is called "signal" (ω_1, with $\omega_1 > \omega_2$) and "idler" (ω_2). Since the efficiency of this process, the optical parametric generation (OPG), is determined by the phase matching condition $\boldsymbol{k}_3 = \boldsymbol{k}_1 + \boldsymbol{k}_2$ the wavelengths of signal and idler can be tuned continuously by controlling the orientation of the non-linear crystal axis with respect to the incident pump beam.

In the present experiment a commercially available system named "TOPAS"[6] (Travelling-wave optical parametric amplifier of superfluorescence) is used and the different steps for the generation of tunable fs-IR pulses are schematically depicted in Fig. 2.7.

In the first step, the optical parametric generation (OPG) a signal and idler pair is generated. Therefore, 1% of the pump pulse is focussed onto a BBO, where due to superfluorescence coherent broadband radiation emerges. Out of this spectrally broad radiation only the desired frequencies ω_1 and ω_2 are amplified in two subsequent steps because of the phase matching condition in the non-linear crystal. Signal and idler can be tuned in the range of ≈ 1.1 to $1.6\,\mu\text{m}$ and ≈ 1.6 to $2.1\,\mu\text{m}$ respectively [Dan93]. Another two amplification steps named OPA1 and OPA2 follow the above described procedure, wherein signal and idler are amplified. OPA2 is strongly saturated, so that pulse-to-pulse fluctuations are minimized. In a final step, the desired mid-IR pulse are obtained from signal and idler via DFG $\omega_{\text{IR}} = \omega_1 - \omega_2$ in a AgGaS$_2$ crystal.

The generated mid-IR pulses are separated with a ZnSe filter and a Ge plate (mounted under the Brewster-angle) from the remaining signal and idler light. Pulse energies up to $30\,\mu\text{J}$ are feasible at $\lambda = 5\,\mu\text{m}$ for instance.
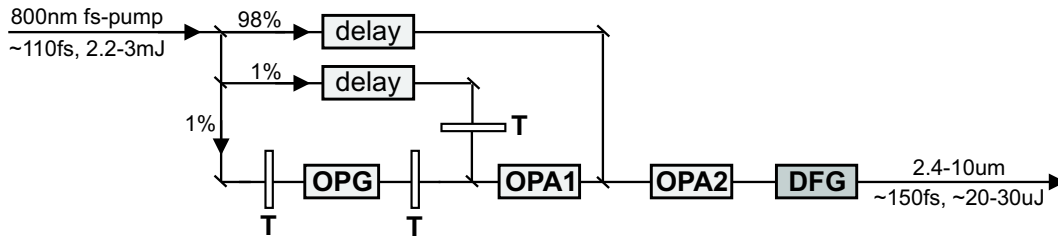

Figure 2.7.: Scheme of the generation and amplification of fs-IR-laser pulses in the TOPAS. The processes named OPG, OPA1 and OPA2 taking place in the same BBO crystal but are sketched separately for a clearer depiction. The radiation generated in these steps lies in the near infrared, which is then via a DFG process transformed into the wanted mid-IR range. T stands for telescope and "delay" for an adjustable delay distance. Figure taken from [Den03a].

2.2.3. Laser pulse characterization

Spectrum and temporal shape of the $800\,\text{nm}$ laser pulses generated by the amplifier system are shown in Fig. 2.8. The spectrum is measured with a commercially available grating spectrometer and shows a bandwidth of $\approx 25\,\text{nm}$. The pulse intensity $I(t)$ is measured via autocorrelation. Therefore, the laser beam under investigation is divided by a beam splitter into two beams, which then are superimposed in a BBO crystal where they interact. This

---

[6]Lightconversion, Vilnius, Lithuania.

interaction leads via second harmonic generation (SHG) to light of 400 nm wavelength, whose intensity $I_{SHG}(\tau)$ is measured as a function of the temporal delay τ between the two pulses. It yields the intensity autocorrelation of the input pulse according to

$$I_{SHG}(\tau) \propto \int I(t) \cdot I(t + \tau)\, \mathrm{d}t. \tag{2.2}$$

As can be seen from Fig. 2.8, the shape of the autocorrelation can be well described with an sech^2 function, wherefore the ratio between the FWHMs of the autocorrelation $\Delta\tau$ and of the pulse duration Δt is given by $\Delta\tau/\Delta t = 1.55$ [Dem98]. For the spectrum of Fig. 2.8, this yields in a pulse duration of ≈ 90 fs. In the following examples, Gaussian intensity distributions $I(t)$ are assumed, since the error due to the differences between the two line shapes is negligible.

The spectrum of the mid-IR pulses at a center frequency of 2000 cm^{-1} generated by the TOPAS is depicted on the left hand side of Fig. 2.9. The spectral width of the IR pulses is typically ≈ 200 cm^{-1}, the center frequency can be varied within the range of ≈ 1900 to 5000 cm^{-1}. The spectrum is measured with a grating spectrograph und the IR light is detected by a liquid nitrogen cooled MCT (mercury cadmium telluride) detector.

The pulse duration is determined by a cross-correlation measurement between the IR- and the 800 nm pulses. To this end sum frequency generation (SFG) is applied by focusing the IR and the 800 nm light onto the Ru(001) surface, which is held at 650 K to avoid resonant adsorbate contributions to the SFG signal (see Section 2.4.4). The SFG spectrum, now only containing non-resonant background contributions, is measured with an intensified CCD, which is mounted to a grating spectrograph. The SFG intensity as a function of the temporal delay between the two pulses is shown on the right hand side of Fig. 2.9. The cross-correlation shows a FWHM of ≈ 380 fs corresponding to an IR pulse duration of ≈ 360 fs, which is obtained by deconvolution of the cross-correlation with the known pulse shape of the 800 nm pulse.

As shown in the foregoing passage, temporal information can be obtained from the SFG light by generating it with two short and therefore inevitably spectrally broad pulses. To gain spectral information, one of the two pulses has to be spectrally narrow (Section 2.4.4). A spectral narrow 800 nm pulse is generated with a pulse shaper, discussed in very detail by Denzler [Den03a] and Hess [Hes01]. Here, only a brief description is given: the non-converted 800 nm light out of the TOPAS is spatially dispersed by a grating and afterwards spectrally cut by a slit (see Fig. 2.22, p. 58). The characteristics of such a typical spectral narrow 800 nm pulse, also named upconversion pulse, is depicted in Fig. 2.10. A spectral width of ~ 0.5 nm at a center frequency of 800 nm is again measured with the grating spectrometer used for characterization of the 800 nm pulses out of the amplifier system (see above). The pulse duration is determined by measuring a crosscorrelation between the short 800 nm pulse and the long upconversion pulse. The FWHM of ≈ 4 ps of the crosscorrelation can be attributed to the pulse length of the narrow band 800 nm pulse. Pulse energies around $8\,\mu$J complete the information.
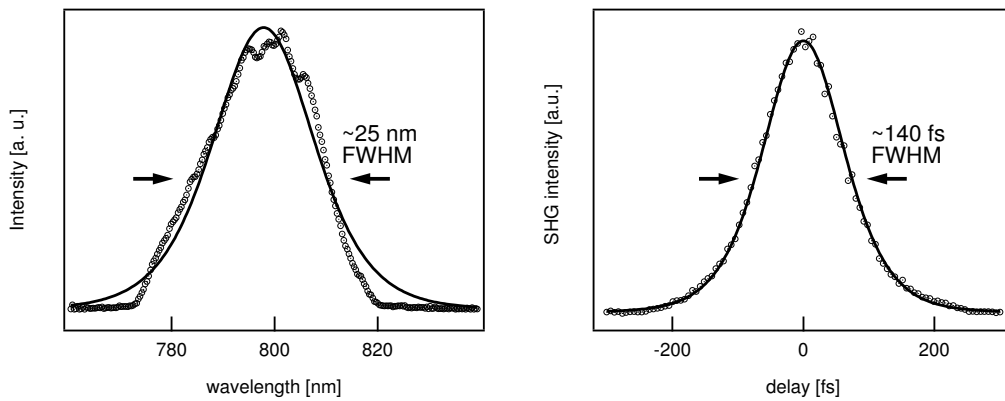
Figure 2.8.: Spectrum and autocorrelation of the amplified laser pulse. Assuming sech^2-shaped pulses (lines) one obtains a spectral FWHM of 25 nm and a pulse duration of ≈ 90 fs by deconvoluting the autocorrelation signal with a ≈ 140 fs FWHM.
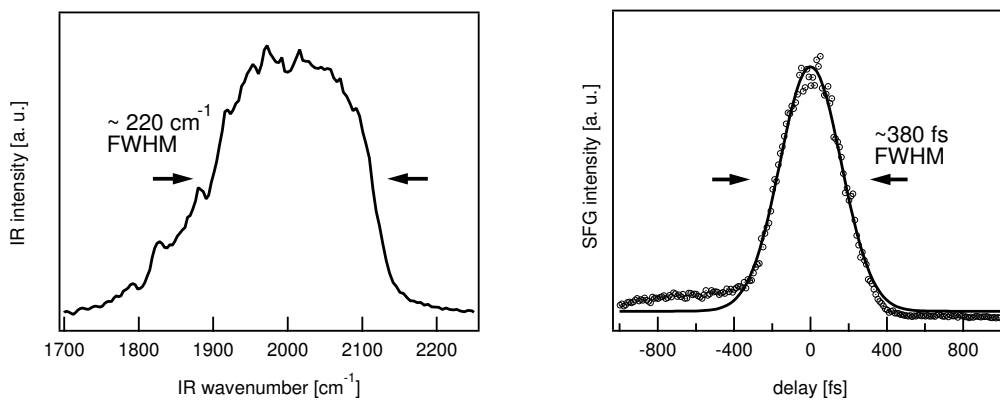

Figure 2.9.: Typical spectrum (left) of and crosscorrelation (right) between the fs-IR-pulse and a ≈ 100 fs 800 nm laser pulse.
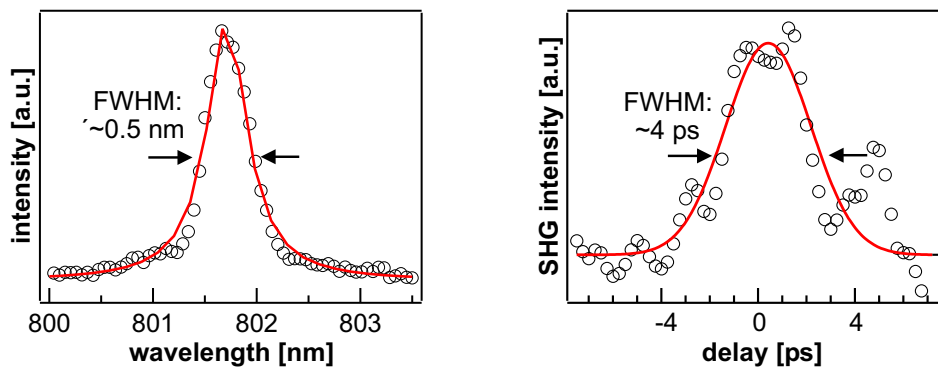

Figure 2.10.: Typical spectrum (left) of and crosscorrelation (right) between the 800 nm upconversion pulse and a ≈ 120 fs 800 nm laser pulse (taken from [Den03a]).

2.3. Dye-laser system and generation of tunable VUV radiation

Tunable narrow-band vacuum[7] ultraviolet (VUV) radiation at the wavelength around 110 nm and also ultraviolet (UV) light are required for the state-resolved detection of D_2 (Section 2.4.3). Therefore an additional dye laser system, schematically shown in Fig. 2.11, was set up. Its details as well as the VUV generation and detection are described in the present section.
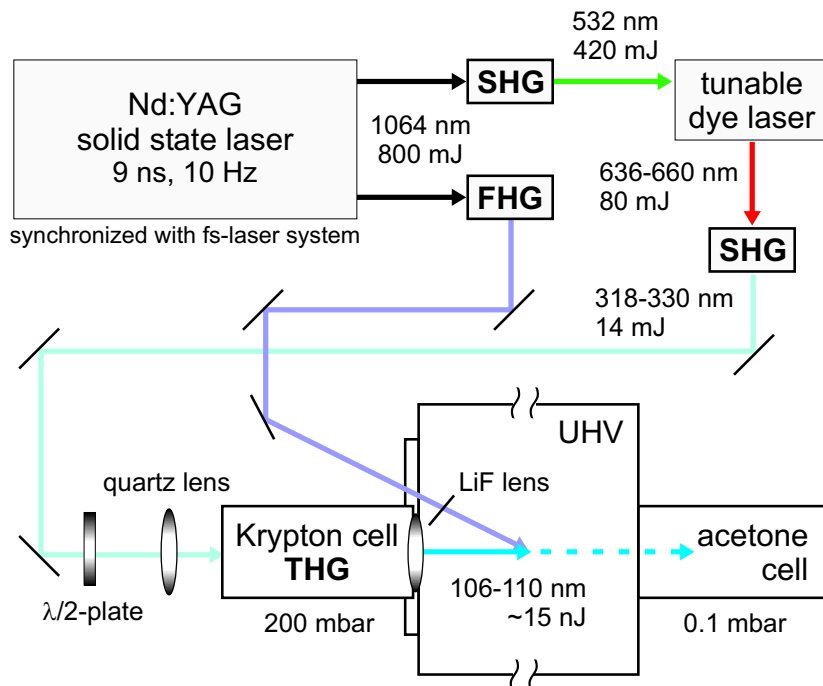

Figure 2.11.: Schematic diagram of the laser system applied for the generation of UV and tunable narrow-bandwidth VUV pulses, including the energies and wavelengths at the different steps of the generation process. SHG, THG and FHG indicate second, third and fourth harmonic generation, respectively.

The dye-laser system operates at 10 Hz repetition rate. Its basis is a solid-state Nd:YAG laser delivering 9 ns pulses, whose frequency doubled radiation of 532 nm is divided into the two beam paths required for the (1+1') REMPI scheme (Section 2.4.3). Along one beam path the laser pulses are again frequency doubled in a KD*P crystal to obtain UV light with a wavelength of 266 nm, whereas a second portion pumps a dye laser. Via a refractive grating inside the dye laser cavity, the wavelength can be tuned in the range from 636 to 660 nm with a spectral width of $\Delta\tilde{\nu} = 0.10\,\text{cm}^{-1}$. The tuning is obtained by motorized computer-controlled rotation of the grating with a minimum wavelength change of 10^{-3} nm. The output of the dye laser is frequency-doubled in a KD*P crystal. In a final step its third harmonic is generated (see below) in a krypton gas cell (200 mbar). A $\lambda/2$-plate in front of the gas cell allows to rotate the polarization of the 318-330 nm light and thereby the polarization of the VUV. The krypton cell was separated from the UHV chamber by an LiF lens transparent in this VUV wavelength range. On the opposite side of the chamber, again separated by a LiF window,

---

[7]Since air is opaque below $\approx 200\,\text{nm}$, vacuum is required for the propagation of light for wavelengths shorter than $\approx 200\,\text{nm}$.

an acetone gas cell ($p = 0.1$ mbar) is mounted, where VUV single photon ionization of the acetone molecules allows monitoring the VUV intensity. The energies of the laser pulses at the different steps of generation are given in Fig. 2.11.

VUV generation

A frequently used method of generating coherent VUV laser radiation is non-resonant frequency tripling in a noble gas. The polarization $\boldsymbol{P}$ induced in the gas is given by

$$\boldsymbol{P} = \chi^{(1)}\boldsymbol{E} + \chi^{(3)}\boldsymbol{E}\boldsymbol{E}\boldsymbol{E} + ..., \tag{2.3}$$

where $\chi^{(i)}$ are the susceptibility tensors and a measure of how easily the medium polarizes in response to the applied electric field $\boldsymbol{E}$ of the fundamental. The second order term vanishes in isotropic media (see 2.4.4) as in atomic or molecular (non-chiral) gases. Since the non-linear susceptibilities $\chi^{(3)}$ for gases are very small, the third order term with its tripled frequency only contributes significantly to the induced polarization when high electric fields are applied. Therefore, the second harmonic of the dye laser output is focused into the gas cell, where in the given setup[8] an intensity of P $\approx 5 \cdot 10^{12}$ W/cm^2 is achieved. For Gaussian beams and laser intensities below $\sim 10^{14}$ W/cm^2 Bjorklund [Bjo75] derived an analytical expression for the generated VUV power P$_{\mathrm{VUV}}$ in the case of strong focusing ($b \ll L$). It can be written in the following form:

$$P_{\mathrm{VUV}} = 8\pi^2 \left(\frac{10^7}{c}\right)^2 \frac{k_{\mathrm{VUV}}k_{\mathrm{UV}}^3}{C^2 b^2} \left|\chi^{(3)}\right|^2 P_{\mathrm{UV}}^3 G^{(3)}\left(b\Delta k, b/L, f/L, k''/k'\right), \tag{2.4}$$

where the phase matching function $G^{(3)}$ is given by

$$G^{(3)}(b\,\Delta k, b/L, f/L, k''/k') = \begin{cases} \pi^2\,(b\,\Delta k)^4 e^{b\,\Delta k} & \text{for} \quad \Delta k < 0 \\ 0 & \text{for} \quad \Delta k \geq 0 \end{cases}. \tag{2.5}$$

C is the wave vector mismatch per atom, b the confocal parameter of the Gaussian beam, L the length of the conversion medium, $\Delta k = k_{\mathrm{VUV}} - 3k_{\mathrm{UV}}$, $k'' = 3k_{\mathrm{UV}}$, and $k' = k_{\mathrm{VUV}} - \Delta k$ with k_{UV} and k_{VUV} the wave vectors of the fundamental UV and the generated VUV radiation, respectively. f is the focal length of the focussing lens. The phase matching function $G^{(3)}$ restricts efficient third-harmonic generation to wavelength regions of negative dispersion($\Delta k < 0$) of the conversion medium. The atomic wave-vector mismatch C per atom is a function of the involved wave vectors k_{UV} and k_{VUV} and given by:

$$C = \frac{\Delta k}{N} = \frac{k_{\mathrm{VUV}} - 3k_{\mathrm{UV}}}{N} = \frac{2\pi}{N\lambda_{\mathrm{VUV}}}\frac{n_{\mathrm{UV}} - n_{\mathrm{VUV}}}{n_{\mathrm{UV}}}, \tag{2.6}$$

where n_i are the refractive indices for the corresponding wavelengths and N is the particle density. Thus, it is possible to optimize the phase matching by adjusting the pressure of the applied gas in the gas cell. A suitable conversion medium for the generation of 110 nm VUV radiation is krypton, wherefore the wave-vector mismatch per atom C is depicted in Fig. 2.12. The required negative dispersion range is indicated by the shaded areas. The conversion efficiency η for the frequency tripling can be estimated as follows [Rut02a]. With respect to

---

[8]λ=330 nm, focal length f=100 mm, beam diameter $\sim$3 mm, pulse duration 9 ns and 14 mJ pulse energy
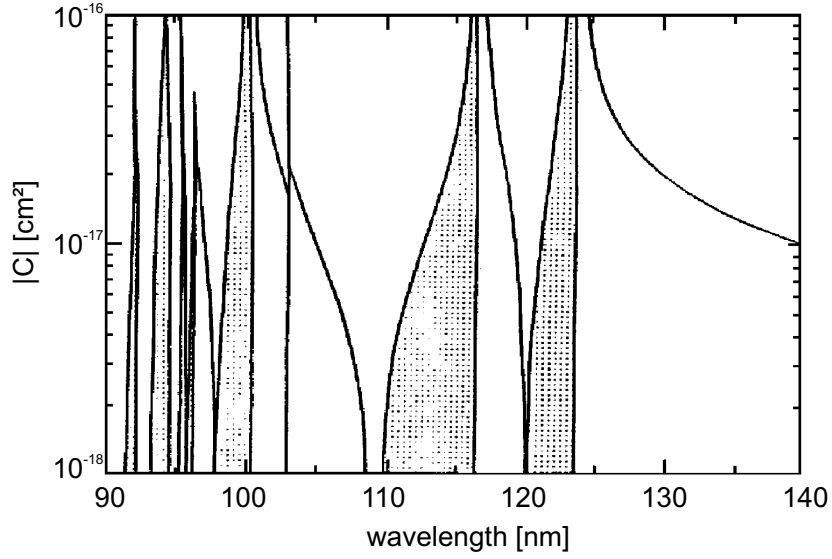
Figure 2.12.: Wave vector mismatch per atom, $\Delta k = CN$ for frequency tripling in krypton as a function of the tripled wavelength. Here N is the number of atoms per cm^3 and n_{UV} and n_{VUV} are the refractive indices at the incident (UV) and tripled (VUV) wavelengths. The shaded areas are regions of negative dispersion required for VUV generation via third harmonic generation. (Figure taken from ([Mah79].)

conversion efficiencies of $\eta = 9 \cdot 10^{-7}$ obtained with half the UV intensity but shorter pulses (2.2 ns) by Zapka et al. [Zap81], one can specify $\eta = 1 \cdot 10^{-6}$ for the presented setup, which results in VUV pulse energies of 15 nJ.

For a more comprehensive discussion about tunable VUV generation see [Rut02a, Jam83].

2.4. Experimental methods

After having presented the different components of the experimental setup in the previous sections, the purpose of this section is to explain the methods which are applied in the performed experiments. An outline of the data analysis is given as well.

2.4.1. Temperature-Programmed Desorption

Temperature-programmed desorption (TPD) procedures are based on the fact that desorption can be thermally activated. Therefore, the desorption rate is measured as a function of the surface temperature T, whereby the adsorbate covered surface with coverage θ is linearly with $\beta = \mathrm{d}T/\mathrm{d}t = $ const and uniformly heated. During the heating process, the desorbing particles leave the surface until the adsorbate is exhausted, and the pressure returns to its initial value, where the TPD was started. The partial pressure of the desorbing gas runs through a maximum at temperature T_{max}. After time t, the final temperature $T_{\mathrm{f}} = T_{\mathrm{in}} + \beta t$ is reached, and the measurement is stopped when all particles have left the surface and a thermal desorption spectrum (TDS) is obtained.

The desorption process is described by the Wigner-Polanyi equation [Chr91]

$$-\frac{\mathrm{d}\theta_i}{\mathrm{d}t} = \nu_i \theta_i^{x_i} \exp\left(-\frac{E_i}{k_{\mathrm{B}}T}\right), \tag{2.7}$$

where x_i is the reaction order for desorption from state i, ν_i is a frequency factor, E_i is the desorption activation energy and θ_i is the surface coverage in state i. A variety of methods are available for deducing values for these parameters from the experimental data [Chr91]. For first order desorption ($x_i = 1$), Redhead [Red62] showed that the activation energy for desorption E_i is related to the peak temperature T_{max} by

$$E_i = k_{\mathrm{B}}T_{\mathrm{max}}\left(\ln\frac{\nu_i T_{\mathrm{max}}}{\beta} - 3.46\right). \tag{2.8}$$

This method is only approximate, relying on a reasonable guess for ν_i, usually $\nu_0 \approx 1 \cdot 10^{13}\,\mathrm{s}^{-1}$ [Chr91], and the independence of ν_i and E_i on coverage. The latter assumption obviously fails as soon as a multiple-peak structure is observed in the TPD spectrum, which can arise either from repulsive lateral interactions between adsorbed species or from a multi-state model, where the adsorbates are bound in different adsorption (binding) states. While in principle all information of x, E_i and $\nu_i(\theta)$ are contained in the desorption peak positions and shapes, in practice it is often difficult if not impossible to unfold this information unambiguously, especially in the case of overlapping spectral features [Daw72, Pis74, Men75]. Therefore, the TDS analysis will be restricted to the usage of Eq. (2.8).

2.4.2. Time-of-flight measurements

To determine the translational energy of a desorbing particle flux the time-of-flight distribution of the particles has to be measured. This is usually done with a QMS, whose ionization volume[9] is in line-of-sight with the surface. Since the detector signal of a QMS with an

---

[9]Usually, such an ionizer is spatially very localized, which gives a defined flight distance.

electron impact ionizer is proportional to the number density $\rho(t)$ of the particles in the ionization region, faster particles are less likely to be detected because of their reduced residence time in the ionizer. To extract the velocity distribution from the TOF spectrum $S(t)$ one therefore has to weight $\rho(t)$ by the velocity v leading to the TOF distribution $I(t) = v\rho(t) \propto t^{-1}S(t)$. From such a TOF distribution one obtains the velocity distribution $P_v(v)$ by setting $I(t)\,\mathrm{d}t = P_v(v)\,\mathrm{d}v$, and using the Jacobian $|\mathrm{d}v/\mathrm{d}t| = r/t^2$, where r is the flight distance yields [Zim95]

$$P_v(v) = \frac{t^2}{r}I(t) \propto \frac{1}{v}S(t). \tag{2.9}$$

Characterization of the translational energy distribution in terms of mean translational energy $\langle E_t \rangle$ or flux weighted mean velocity $\langle v \rangle$ is very convenient by introducing the moments M_n of the normalized velocity distribution $P_v(v)$ [Zim95, Has95]:

$$M_n = \int v^n P_v(v)\,\mathrm{d}v = \frac{r^n \int t^{-(n+1)}S(t)\mathrm{d}t}{\int t^{-1}S(t)\mathrm{d}t}. \tag{2.10}$$

In terms of these moments, the mean translational energy can be expressed as

$$\langle E_t \rangle = \int E_t P_v(v)\mathrm{d}v = \frac{1}{2}mM_2, \tag{2.11}$$

a quantity *directly* accessible from the experimental data. $\langle E_t \rangle$ can be related to a temperature T_t, if the velocity $P_v(v)$ is Maxwell-Boltzmann like. A *flux-weighted* Maxwell-Boltzmann distribution, which has to be considered for thermal desorption from a surface with unit sticking probabilty [Com85] and for MGR-type photodesorption[10] [Zim94], is given by [Rei65]

$$P_v(v)\,\mathrm{d}v = \frac{1}{2}\left(\frac{m}{k_B T}\right)^2 v^3 \exp\left(-\frac{mv^2}{2k_B T}\right)\,\mathrm{d}v, \tag{2.12}$$

and is characterized by $\langle E \rangle = 2k_B T$. Due to phase space considerations, this expression changes to $\langle E \rangle = k_B T$ when desorption only occurs in one dimension, as for example in the calculations by Luntz et al. [Lun06] discussed in Section 3.4.

The empirical formula used to fit the the experimental velocity distributions is the so-called *modified* Maxwell-Boltzmann distribution

$$P_v(v)\,\mathrm{d}v \propto v^3 \exp\left(-\frac{m(v-v_0)^2}{2k_B T}\right)\,\mathrm{d}v, \tag{2.13}$$

which can be interpreted as a thermal distribution at temperature T, superimposed on a stream velocity v_0, which reduces to Eq. (2.12) for $v_0 = 0$. The purpose of the stream velocity is to make the reduced width of the distribution an adjustable quantity.

By modeling the measured data with Eq. (2.13), one can test, if its characterization with a single temperature T_t is justified or if multiple *modified* Maxwell-Boltzmann distributions are required. This would indicate the existence of several reaction channels, characterized by different temperatures T_t, which then sum up to the overall mean translational energy $\langle E_t \rangle$ obtained from the raw data.

---

[10]see Section 1.1.4

2.4.3. State-resolved detection of D_2 via REMPI

To gain microscopic insight into the D_2 desorption process (Chapter 3), it is essential to have information about the energy transfer to the different internal degrees of freedom of the formed molecule. This information corresponds to the knowledge of the population of the different molecular rotational and vibrational quantum states, which is accessible by means of laser spectroscopy, namely the resonance enhanced multi-photon ionization (REMPI). A short explanation of this technique is given first and afterwards related to the electronic band spectrum of D_2. Since the applied (1+1') REMPI scheme also offers the opportunity of detecting the molecular alignment, a paragraph concerning this topic ends the section.
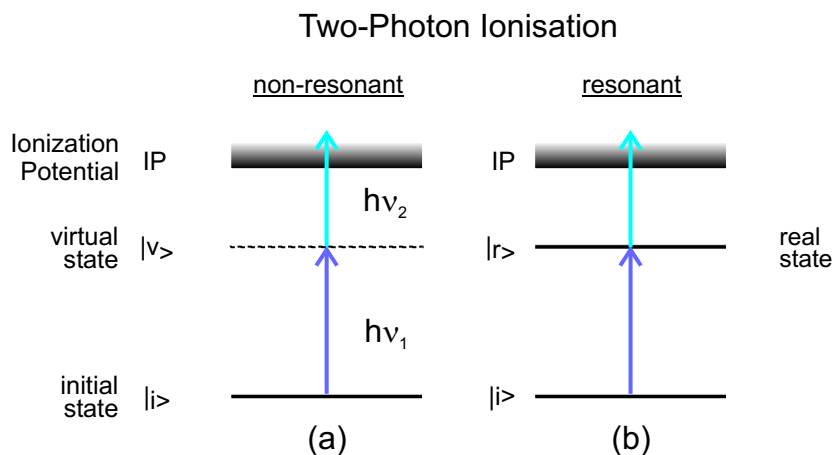

Figure 2.13.: Level schemes for different two-photon ionizations: (a) non-resonant ionization via a *virtual* state $|v\rangle$ and (b) resonant absorption by a *real* intermediate state $|r\rangle$. The REMPI principle is that a *real* intermediate state $|r\rangle$ at resonance drastically increases the ionization yield.

REMPI

The REMPI principle is sketched in Fig. 2.13 for the special case of a two-photon ionization with two different photon energies[11]. Two-photon ionization may occur by a non-resonant excitation via a *virtual* state $|v\rangle$ (Fig. 2.13a) or resonant via a *real* intermediate state $|r\rangle$ (Fig. 2.13b). The resonant excitation enhances the ionization by a factor of 10^4 to 10^6 [Goo92], so that resonant transitions can be probed with high sensitivity [Par83]. If the intermediate state $|r\rangle$ is unpopulated and the ionization step saturated for all $|r\rangle$[12], the measured ion signal is directly proportional to the ground state population. In molecules, the electronic states show a rovibrational substructure, and resonant transitions between those electronic bandlike states are in general unambiguously correlated to distinct rovibrational quantum numbers in the ground and the excited state. This means that the REMPI yield I_{ion} of a known resonant

---

[11]This is the so-called (1+1') REMPI, where the numbers denote single (1) photon excitation steps and the apostrophe indicates a different photon energy

[12]These conditions are fulfilled in the present experiment, since the D_2 molecules are in the electronic ground state and the photon density for ionization is $\sim 10^6$ higher than for resonant excitation. The saturation of the ionization was also checked experimentally by Rutkowski et al. [Rut02a].

excitation can be directly correlated to a ground state population $N(v'', J'')$ via

$$N\left(v'', J''\right) \propto \frac{I_{\text{ion}}}{w_{n''v''J''}^{n'v'J'}}, \tag{2.14}$$

with $w_{n''v''J''}^{n'v'J'}$ the transition probability for electronic excitation from the ground state $|n''v''J''\rangle$ to the excited state $|n'v'J'\rangle$. The transitions are denoted by $(v'v''\,[\text{P or R}]\,J'')$ with the vibrational and rotational quantum number v and J, respectively. P or R indicate the rotational branch (see below). With this notation all involved rovibrational quantum numbers are described.
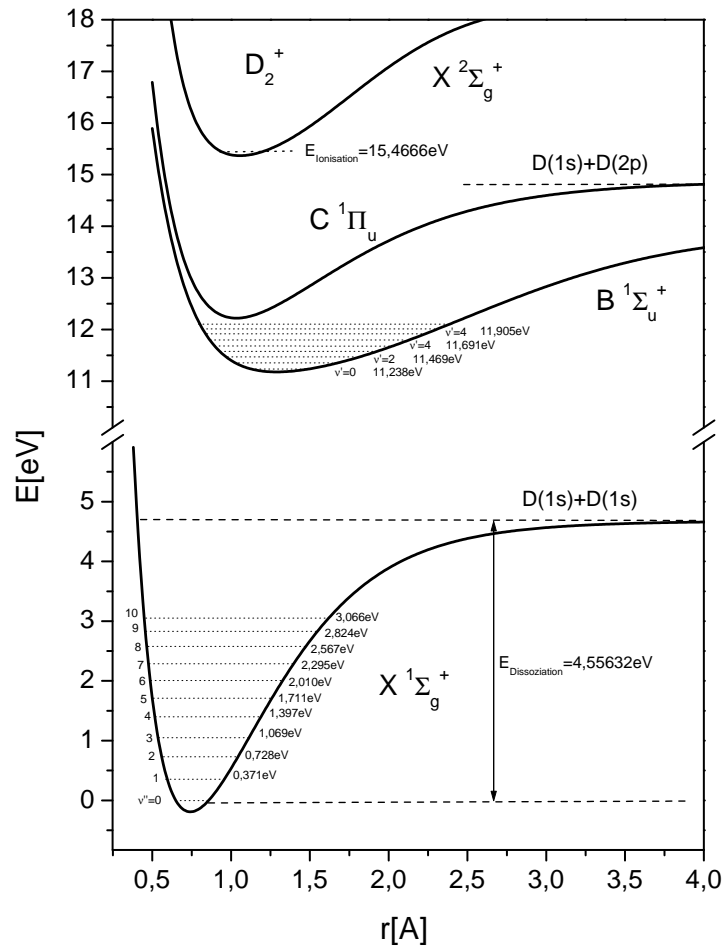
Electronic structure of D_2

Figure 2.14.: Potential energy curves for D_2 and D_2^+. Shown are the vibrational levels in the electronic ground state $X^1\Sigma_g^+$ and the first excited state $B^1\Sigma_u^+$, in-between which the resonant excitation step of the REMPI process took place. With courtesy of M. Rutkowski taken from [Rut02a].

The electronic structure of D_2 is given in Fig. 2.14. The rotational sublevels J of the vibrational levels v are not shown. The resonant excitation required for the REMPI scheme

involves the electronic ground state $X^1\Sigma_g^+$ and the first electronically excited state $B^1\Sigma_u^+$. Photon energies around $\sim 11.5\,\text{eV}^{13}$ are required for excitation, as can be seen in Fig. 2.14. The probability for such an excitation is determined by three factors, corresponding to the electronic, vibrational and rotational fraction in the overall transition probability and given by [Kov69]

$$w_{n''v''J''}^{n'v'J'} = \left| R_{\text{el}}^{n'n''} \right|^2 \left| R_{\text{vib}}^{v'v''} \right|^2 S_{J'J''}. \tag{2.15}$$

Here, $\left| R_{\text{el}}^{n'n''} \right|$ denotes the electronic transition moment between the electronic states n'' and n', whereas *Franck-Condon* factor $\left| R_{\text{vib}}^{v'v''} \right|$ describes the overlap between the vibrational wave functions of the involved vibrational states. Finally, $S_{J'J''}$ denotes the *Hönl-London* factor, which depends on the angular momenta and their orientation in space. For the quantitative analysis of the obtained REMPI spectrum (see Section 3.2.2), the knowledge of the two latter factors in Eq. (2.15) is required, whereas $\left| R_{\text{el}}^{n'n''} \right|$ does not have to be known, since the electronic transition is the same for all excitations occuring between the same electronic states. Note that a transition can only happen, if none of the three factors is zero. For the $\Sigma \leftarrow \Sigma$ transition that is investigated, only P- and R-bands with $\Delta J = \pm 1$ are allowed, since otherwise the *Hönl-London* factor vanishes. No restrictions have to be taken into account with respect of Δv.
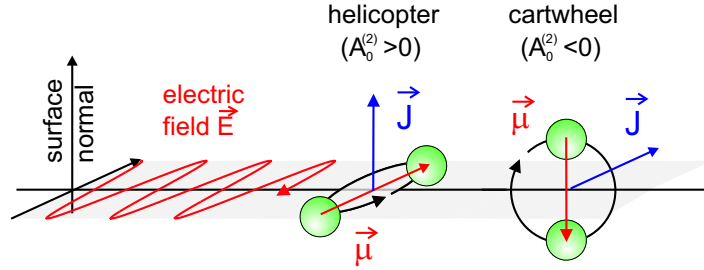
Molecular alignment

Figure 2.15.: Molecular alignment with respect to the surface normal $\boldsymbol{n}$ is shown. Molecules with $\boldsymbol{J} \parallel \boldsymbol{n}$ are called *helicopter*-type, whereas molecules with $\boldsymbol{J} \perp \boldsymbol{n}$ are termed *cartwheel*-type. The vector $\boldsymbol{\mu}$ denotes the transition dipole moment. The excitation with polarized light is shown and differences with respect to the molecular orientation are discussed in the text.

Since the transition probability given in Eq. (2.15) depends on the geometric orientation of the D$_2$ molecule, it is possible to measure the molecular alignment with a (1+1') REMPI scheme [Jac86]. For P- and R- transitions, the electronic transition dipole moment (now denoted $\boldsymbol{\mu}$) lies in the plane of rotation. By varying the polarization of the excitation light, it is possible to measure the alignment, since the excitation probability depends on the angle between $\boldsymbol{\mu}$ and the electric field $\boldsymbol{E}$, with a maximum for $\boldsymbol{\mu} \parallel \boldsymbol{E}$ and a minimum for $\boldsymbol{\mu} \perp \boldsymbol{E}$. The examples depicted in Fig. 2.15 illustrate these two cases, where the molecules with the angular momentum vector $\boldsymbol{J}$ are aligned with respect to the surface normal $\boldsymbol{n}$. For the *helicopter*-type molecules ($\boldsymbol{n} \parallel \boldsymbol{J}$) excitation with light polarized parallel to surface normal leads to a maximum excitation and a maximum ion signal $I_\parallel$, whereas the *cartwheel*-type

---

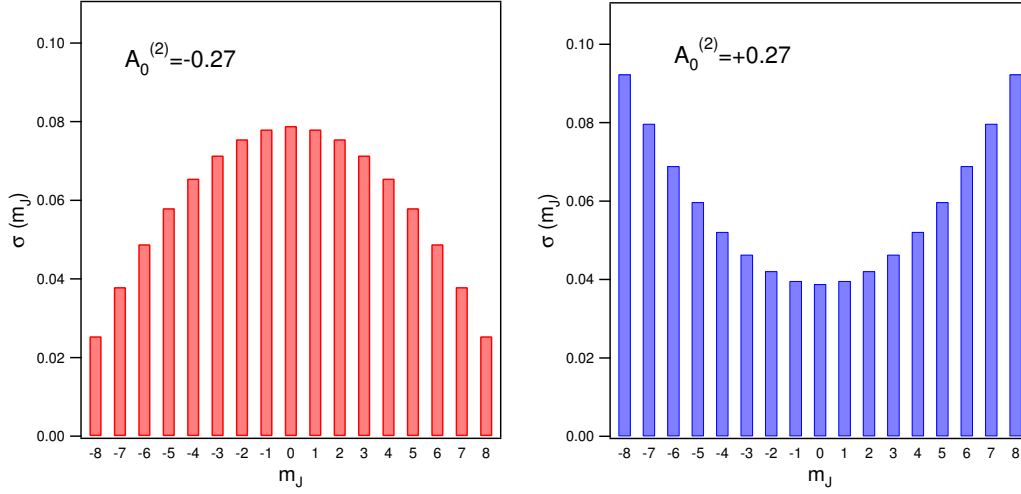[13]equivalent to a wavelength of $\sim 110\,\text{nm}$ (see Section 2.3)

Figure 2.16.: m_J distribution population $\sigma(m_J)$ for two given alignments $A_0^{(2)} = \pm 0.27$. The m_J are the projection $\boldsymbol{J}$ onto the the surface normal $\boldsymbol{n}$. The negative alignment shown in the left diagram corresponds therefore to *cartwheel*-like rotation, whereas on the right an example for positive alignment and a *helicopter*-like rotation is shown.

$(\boldsymbol{n} \perp \boldsymbol{J})$ species are not excited and thus $I_\perp$ vanishes[14]. This means that a change in the polarization with respect to the surface normal allows to determine a possible initial molecular alignment resulting out of the desorption process under investigation. A suitable quantity is the molecular polarization

$$P = \frac{I_\| - I_\perp}{I_\| + I_\perp}, \tag{2.16}$$

which allows to derive the molecular alignment $A_0^{(2)}$ for the P and R branches by the following relations [Gre82]

$$A_0^{(2)} = \frac{-4P\,(2J_i - 1)}{(J_i + 1)\,(3 - P)} \qquad \text{(P branch)} \tag{2.17a}$$

and

$$A_0^{(2)} = \frac{-4P\,(2J_i + 3)}{J_i\,(3 - P)} \qquad \text{(R branch)}. \tag{2.17b}$$

$A_0^{(2)}$ can be correlated to a population distribution $\sigma\,(m_J)$ of the quantized $(2J + 1)$ values for m_J, which are obtained from the projection of $\boldsymbol{J}$ onto $\boldsymbol{n}$. The alignment is then given by [Rut02a]

$$A_0^{(2)} = \sum_{m_J} \frac{3m_J^2 - J\,(J + 1)}{\sqrt{J\,(J + 1)}}\,\sigma\,(m_J). \tag{2.18}$$

Under the assumption of a parabolic distribution $\sigma\,(m_J)$ the population distribution is defined by the alignment. An example is given in Fig. 2.16. Two population distributions $\sigma(m_J)$ are shown. On the left hand side a negative alignment of $A_0^{(2)} = -0.27$ is shown, whereas on the right hand side the situation for $A_0^{(2)} = +0.27$ is depicted. The latter implies that in

---

[14]This simplified picture does not take into account any quantum mechanical effects and is therefore only meant to illustrate the general physics of the polarization dependence on the transition probability. For a detailed discussion see [Zar88].

this example about three quarters, $(74 \pm 6)\,\%$, of the molecules desorb with $|M_{J''}| \geq J''/2$, i.e. in a more helicopter-like rotation, and one quarter, $(26 \pm 6)\,\%$, with $|M_{J''}| < J''/2$ in a *cartwheel*-like motion.

2.4.4. Vibrational spectroscopy via infrared-visible SFG

Surface vibrational spectroscopy is a powerful tool to characterize molecular adsorbates. For this reason, many techniques have been developed [Wil80]. However, most of them suffer from poor sensitivity as well as low spectral and temporal resolution. In contrast, infrared-visible sum-frequency generation (IR-VIS SFG) is highly sensitive, surface specific and capable of achieving high temporal and spectral resolution [She89].

SFG is based on the circumstance that intense optical fields interact in a non-linear way with matter. Because of that, the polarization $\boldsymbol{P}$ does not only depend linearly on the electric field $\boldsymbol{E}$ but also on higher order terms:

$$\boldsymbol{P} = \chi^{(1)}\boldsymbol{E} + \chi^{(2)}\boldsymbol{E}\boldsymbol{E} + \chi^{(3)}\boldsymbol{E}\boldsymbol{E}\boldsymbol{E} + \dots . \tag{2.19}$$

Here, $\chi^{(i)}$ denote the susceptibility tensors. SFG is a second order process. In dipole approximation, $\chi^{(2)}$ vanishes in media with space-inversion symmetry (SIS)[15] [She84]. Since SIS is broken at surfaces and interfaces, SFG is well suited for the investigation of adsorbates. The energetics of the SFG process are depicted in Fig. 2.17. Two different electric fields $\boldsymbol{E}(\omega_{\mathrm{IR}})$ and $\boldsymbol{E}(\omega_{\mathrm{VIS}})$ induce the non-linear polarization

$$\boldsymbol{P}^{(2)}(\omega_{\mathrm{SFG}} = \omega_{\mathrm{IR}} + \omega_{\mathrm{VIS}}) = \chi_{\mathrm{S}}^{(2)}(\theta)\,\boldsymbol{E}(\omega_{\mathrm{IR}})\boldsymbol{E}(\omega_{\mathrm{VIS}}), \tag{2.20}$$

where $\chi_{\mathrm{S}}^{(2)}(\theta)$ is the coverage θ dependent surface susceptibility. The induced polarization $\boldsymbol{P}^{(2)}$ itself acts as a source for the electric fields $\boldsymbol{E}_{\mathrm{SFG}}$, whose intensity is given by [She84]

$$I_{\mathrm{SFG}} \propto \left|\boldsymbol{P}^{(2)}(\omega_{\mathrm{SFG}})\right|^2 \propto \left|\chi_S^{(2)}(\theta)\right|^2 I_{\mathrm{IR}}I_{\mathrm{VIS}}. \tag{2.21}$$

$\chi_{\mathrm{S}}^{(2)}(\theta)$ exhibits a resonant enhancement and can be separated into its resonant and a non-resonant contribution [She84, Hun87]

$$\chi_{\mathrm{S}}^{(2)}(\theta) = \chi_{\mathrm{NR}}^{(2)}(\theta) + \chi_{\mathrm{R}}^{(2)}(\theta) . \tag{2.22}$$

The resonant susceptibility $\chi_{\mathrm{R}}^{(2)}(\theta)$ for molecules adsorbed on the surface can be given by the summation over the mean molecular polarizabilities β_v for all resonances v [Hun87]:

$$\beta_{q,lmn}^{(2)} \propto \frac{\langle g \left| er_n \right| v\rangle}{\hbar\left(\omega_{IR} - \omega_v + \mathrm{i}\Gamma_v\right)}\, R_{lm} \tag{2.23}$$

$$\text{with} \quad R_{lm} = \sum_s \left(\frac{\langle v \left| er_m \right| s\rangle \langle s \left| er_l \right| g\rangle}{\hbar\left(\omega_{SFG} - \omega_{|s\rangle-|g\rangle}\right)} - \frac{\langle v \left| er_l \right| s\rangle \langle s \left| er_m \right| g\rangle}{\hbar\left(\omega_{SFG} + \omega_{|s\rangle-|g\rangle}\right)}\right) . \tag{2.24}$$

---

[15]This can be easily shown by applying the space-inversion operator $\hat{I}$ to $\boldsymbol{P} = \chi^{(2)}\boldsymbol{E}\boldsymbol{E}$: $\hat{I}\boldsymbol{E}\boldsymbol{E} = \boldsymbol{E}\boldsymbol{E}$. $\hat{I}\boldsymbol{P} = -\boldsymbol{P}$ is only satisfied for $\chi^{(2)} = 0$.
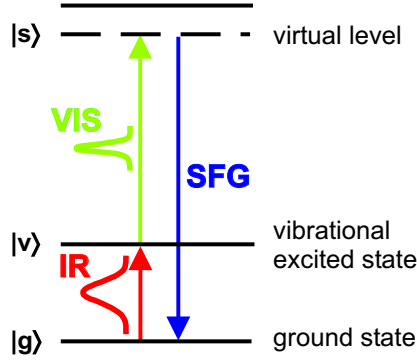
2. Experimental Details

Figure 2.17.: Illustration of the SFG process via a three-level-system composed of the ground state $|g\rangle$, vibrational state $|v\rangle$ and virtual level $|s\rangle$. A (broadband) IR-pulse induces an IR polarization, which is up-converted via a (narrow-band) VIS-pulse. If $|s\rangle$ is a virtual level, the resulting SFG spectrum is dominated by the IR resonance.

$|g\rangle$, $|v\rangle$ and $|s\rangle$ are the ground state, the vibrationally excited state, and the intermediate state according to Fig. 2.17. Equation (2.23) is dominated by the denominator, which describes the resonance between the incident IR frequency ω_{IR} and the vibrational transition ω_v with its corresponding damping constant Γ_v. As can be seen from Eq. (2.23) and Eq. (2.24), the investigated vibrational mode has to be IR-active ($\langle g\,|er_n|\,v\rangle \neq 0$) as well as Raman-active ($R_{lm} \neq 0$) to contribute to the SFG signal [Rei95].

The IR-VIS SFG spectroscopy exploits the resonant contribution of the vibrational state $|v\rangle$ to gather spectroscopic information on the adsorbate. Since $|s\rangle$ is not in resonance with any electronic transition, the SFG intensity can be described by [Hun87]

$$I_{\mathrm{SFG}} \propto \left| |A_{\mathrm{NR}}(\theta)| + \sum_v \frac{|A_v(\theta)|\,\mathrm{e}^{\mathrm{i}\phi_v}}{\omega_{\mathrm{IR}} - \omega_v + \mathrm{i}\Gamma_v} \right|^2 I_{\mathrm{IR}}, \qquad (2.25)$$

with A_{NR} and A_v describing the strength of the non-resonant and spectrally flat background and the resonant contribution of the vibrational modes v, respectively. The ϕ_v's take into account phase shifts between the v resonant and non-resonant contributions.

2.5. Performed experiments

Having discussed details of the experimental components as well as the applied experimental methods in the previous sections, the purpose of this section is to sketch the realization of the performed experiments. This section is ordered with respect to the systems under investigation, namely the fs-laser induced recombinative desorption of D_2 in the first and the one of CO in the latter part. The definition of two important quantites, namely the yield-weighted fluence and the first shot yield are given in the beginning.

Yield weighted fluence

A common issue of fs laser induced reactions is the importance of detailed knowledge about the reaction-inducing laser pulse. The pulse length is characterized as described in Section 2.2.3, whereas the transverse energy distribution, i.e. the beam profile, is measured with a CCD camera. Since typically the reaction yields depend non-linearly on the laser fluence, the concept of a yield-weighted fluence $\langle F \rangle$ (or YWF) is introduced. With the aid of the measured beam profile, the fluence for each camera pixel i is determined and the contribution Y_i to the overall yield is given via

$$w_i = Y_i \propto F_i^n. \tag{2.26}$$

The non-linearity of the yield is taken into account by weighting the averaging with w_i, which then gives

$$\langle F \rangle = \frac{\sum w_i F_i}{\sum w_i} = \frac{\sum Y_i F_i}{\sum Y_i} = \frac{\sum F_i^{n+1}}{\sum F_i^n}, \tag{2.27}$$

where summation takes place over all camera pixels i. If the exponent n is unknown, it is self-consistently fitted to the measured fluence dependence (see Section 4.2).

First shot yield

The first shot yield (FSY) is the most interesting quantity for the investigation of the reaction dynamics. It is obtained as follows:

The measured quantity of the fs-laser induced surface reaction is a time-of-arrival (TOA) distribution of the desorbing particle flux at the mass spectrometer. An exemplary TOA spectrum is shown in the inset of Fig. 2.18. The time-integral over the background corrected distribution results in the yield of the surface reaction. The main graph of Fig. 2.18 shows the decay of the reaction yield with increasing number of laser pulses irradiated onto the surface. As will be discussed in detail in Section 4.2.2, this decay can be fitted via a decay function, which depends on the reaction order. The first shot yield (FSY) of the reaction is then given by the extrapolation of the fit to the first shot. This procedure reduces substantially fluctuations of the measured first shot yield.
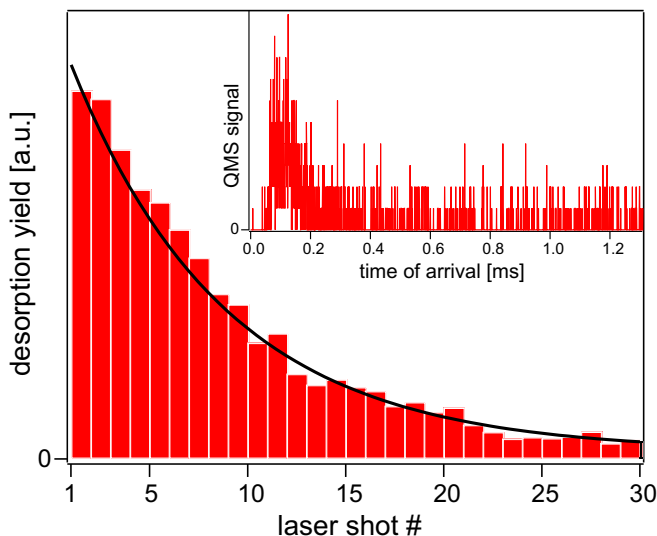
Figure 2.18.: Decay curve of the fs-laser induced desorption yield as a function of the laser number within a series of 30 pulses. The yield for each laser shot is given by the time-integral of the background-free time-of-arrival distribution, the quantity measured in the experiment and exemplarily depicted in the inset. The line represents a fit to the experimental data, which depends on the reaction order of the desorption process.

2.5.1. Investigation of the D_2 desorption energetics

Sample preparation

The Ru(001) crystal is heated very fast ($\approx 40\,\mathrm{K/s}$) to a temperature of $1530\,\mathrm{K}$ by electron bombardment. This so-called "flash" assures that no adsorbates stick to the surface. Afterwards the sample cools down to $170\,\mathrm{K}$ and a deuterium (or hydrogen) saturation coverage is prepared by dosing $50\,\mathrm{L}$ D_2 (H_2) [Feu85]. Before irradiating the prepared sample with laser pulses, the sample is cooled down to $100\,\mathrm{K}$ and moved to the desired position inside the UHV chamber and the laser beam is characterized. Its energy and beam profile are measured in the reference beam path at a position corresponding to the position of the Ru(001) surface in the UHV chamber.

Time of flight measurements

The experimental setup applied for measuring the D_2 (H_2) TOF spectra is depicted in Fig. 2.19. The sample is irradiated with single $800\,\mathrm{nm}$ fs-laser pulses under an angle of $45°$. The crystal surface normal is pointing directly to the ionization volume of the QMS used for detection. The amplified QMS signal is recorded in a time-resolved manner with a multichannel scaler synchronized to the reaction driving laser pulse. From the so-obtained time-of-flight (TOF) spectra the drift time t_0 through the ion optics and the quadrupole mass filter has to be subtracted. t_0 is determined by measuring TOF spectra for two different sample-ionizer distances (160 and $190\,\mathrm{mm}$). The $20\,\mathrm{Hz}$ repetition rate of the laser system in combination with a computer-controlled and synchronized shutter allows to measure the TOF spectra for single laser pulses. For a more detailed description of the data acquisition procedure see [Den03a].
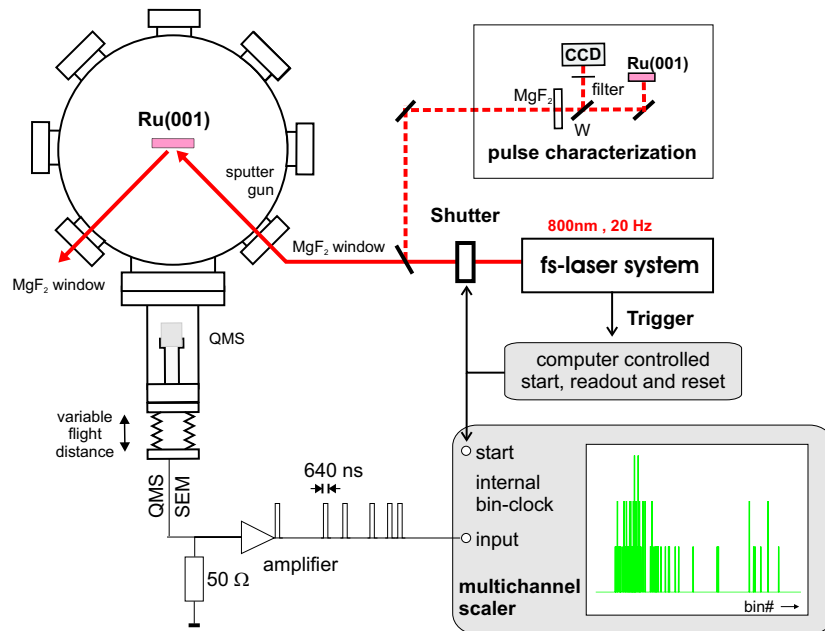
Figure 2.19.: Schematic view of the setup, which was used to perform the D_2-TOF measurements. Shown are the UHV chamber equipped with a moveable QMS, the reference beampath for laser pulse characterization and the data acquisition scheme, which allows measuring single-shot TOF spectra.
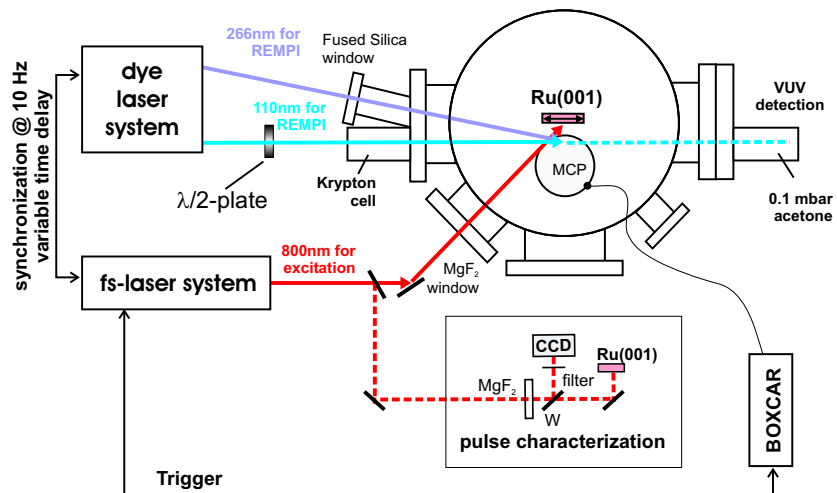

Figure 2.20.: Schematic diagram of the experimental components used for the state-resolved detection of fs-laser induced D_2 desorption from Ru(001). The two laser systems (see Section 2.2 and Section 2.3) are synchronized with a variable time delay. A reference beampath for laser pulse characterization is shown, as well as the data acquisition performed via a triggered boxcar integrator measuring the REMPI signal amplified by a MCP detector.

REMPI

The scheme applied to perform the state-resolved detection of the desorbing D_2 molecules is depicted in Fig. 2.20. The two laser systems (see Section 2.2 and Section 2.3) are synchronized at a repetition rate of 10 Hz. The focused fs-laser beam (diameter 0.5 mm) is scanned over the deuterium-covered ruthenium surface by moving the crystal via computer-controlled stepper motors. In order to detect the desorbing D_2 molecules, the UV and VUV laser beams are overlapped under an angle of 12° in a plane parallel to the crystal surface at a focus 10 mm in front of the crystal. The temporal delay between the fs and the VUV laser is adjusted that only molecules at the maximum of the TOF spectrum are ionized. For the absorbed laser fluence of $85\,\mathrm{J/m^2}$ this corresponds to a delay of $2.4\,\mu$s.

For each laser shot, the REMPI signal is amplified by a MCP detector and recorded with a boxcar integrator. For normalization, the MCP background level and the VUV intensity are recorded with another set of boxcar integrators, not shown in Fig. 2.20. The population distribution is measured by tuning the VUV wavelength (see Section 2.3) over the relevant excitation wavelength range during one single scan over the prepared Ru(001) surface. Measurements of the molecular alignment are performed by changing the VUV polarization with a $\lambda/2$-plate between two consecutive surface scans.

A detailed description of the data acquisition procedures can be found in [Rut02a].

2.5.2. Investigation of the CO reaction dynamics

Sample preparation

To investigate the recombinative desorption of CO from a Ru(001) surface, both species, carbon and oxygen, have to adsorb atomically. Before each preparation, the Ru(001) crystal is "flashed" with the electron beam bombardment to 1530 K for 10 s. When the crystal cooled down to 500 K, ethylene is dosed either via the pinhole doser or a background leak valve. Afterwards, short heating to 650 K is done to decompose the adsorbed C_2H_4 [Hrb85, Liv00] and to form surface carbon. Then the crystal is cooled to 400 K and 8 L of oxygen are dosed, which gives a (2×1) saturation coverage of atomically bound oxygen [Kos92]. Usually, $^{18}O_2$ is used for the preparation to minimize the CO background level of the QMS signal, since $^{12}C^{18}O$ is not part of the residual gas, whereas $^{12}C^{16}O$ is. All experiments were performed at a sample temperature of 400 K, which is above the desorption temperature for molecular CO on a (2×1)O/Ru(001) surface [Kos92]. This assures additionally that the CO detected in the various experiments results from formation on the surface.

Thermal desorption spectroscopy

The TDS and the TPO (temperature programmed oxidation) spectra respectively were measured with the Feulner cup (see Section 2.1). Therefore, the sample with the prepared adsorbate structure is moved in front of the Feulner cup, and the crystal is linearly and uniformly heated by resistive heating. The temperature, the partial pressures of the desorbing species[16] and the time are recorded during heating.

---

[16]By switching the mass filter of the QMS during the TPD, it is possible to record up to four masses within one run.

Time-of-flight and desorption yield measurements

The setup used for these experiments is depicted in Fig. 2.21. The repetition rate of the laser system is decreased to 20 Hz, which in combination with a computer-controlled shutter in the beam path, allows irradiation of the sample with a single laser pulse. The laser beam hits the surface under an angle of 45° and is characterized before performing the experiments in the reference-beam path. The surface normal points towards the ionization volume of the QMS. The intrinsic ion drift time t_0 inside the QMS is measured by laser induced desorption of CO from the ionizer. The mass filter of the QMS can be changed between consecutive laser shots. Integration of the data results in the reaction yield normal to the surface. For several spots on the prepared Ru(001) surface, the yield as a function of laser shots is recorded according to the data acquisition described in Section 2.5.1.

The desorption is either investigated with a single pulse excitation, where in addition to 800 nm light also frequency doubled 400 nm light is used, or with a 2-pulse correlation scheme. For the latter, the reaction inducing laser beam is divided into two beams by a 50% beam splitter. The time delay between the two pulses is set by a computer controlled delay stage. Temporal overlap t_0 between the two pulses is assured by maximizing the SHG intensity obtained from the BBO crystal in the reference beam path. To avoid pulse interference at $t = 0$ at the Ru(001) surface, a $\lambda/2$-plate rotates the polarization of one of the two beams perpendicular with respect to the other one.

Time-resolved vibrational spectroscopy via SFG

The experimental setup applied for the time-resolved investigation of the CO formation is shown in Fig. 2.22. The three required laser beams (IR, VIS and pump) irradiate the Ru(001) crystal under an angle of $\approx 75°$ with respect to the surface normal, which is pointing towards the ionizer of the QMS. The temporal delay between the short 800 nm pump and the short IR pulse can be set with a delay stage. Time zero $t = 0$ and the spatial overlap between the three pulses is assured by maximizing the SFG intensity for the IR and VIS beams and the IR and pump beams, respectively. The LiIO$_3$ reference crystal is placed outside the UHV chamber corresponding to the position of the Ru(001), so that the spatial and temporal overlap can be easily controlled. The generated SFG light is discriminated against residual 800 nm light and then focused onto the entrance slit of a spectrograph. It is detected by an intensified CCD camera. The intensifying high voltage pulses are synchronized to the 400 Hz repetition rate of the laser system and are computer activated. This, in combination with a fast computer-controlled shutter in the pump beam path, allows to record the IR-VIS SFG signal from the Ru(001) surface with and without a pump pulse inducing the CO formation. Since the two 800 nm beams are not collinear, the generated SFG light either from the VIS or the pump are spatially separated. For the experiment, only SFG light generated from the narrow-band VIS beam is detected.

The measurement scheme is as follows: The Ru(001) crystal is moved via computer controlled stepping motors parallel to its surface plane while scanning the Ru crystal. This assures that the generated SFG light does not walk off in space. Around 50 spots on the Ru(001) surface are irradiated. For each spot up to five measurement cycles are performed. Each cycle consists
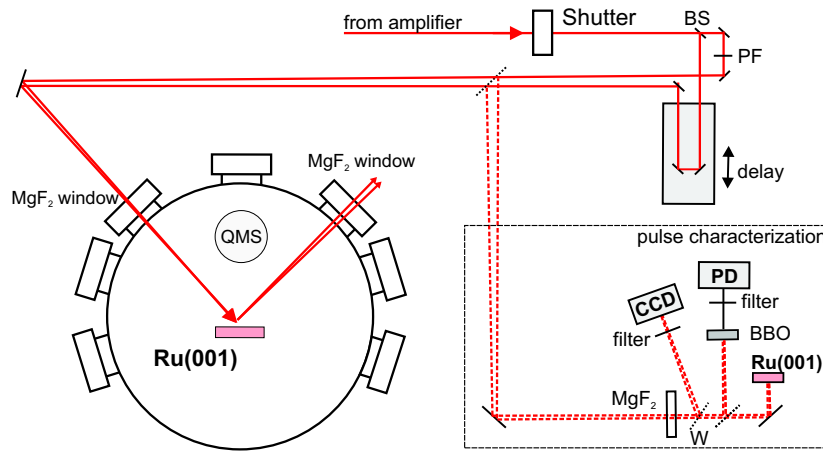
2. Experimental Details

Figure 2.21.: Scheme of the setup used for the investigation of the fs-laser induced recombinative CO desorption. Depending on the measurement type, a single or two time-delayed and perpendicularly polarized laser pulses irradiate the Ru(001) surface. The reference-beam path allows to determine the time delay and the spatial overlap of the two pulses. Experiments are performed either with 400 or 800 nm pulses. Data acquisition is performed as shown in Fig. 2.19.
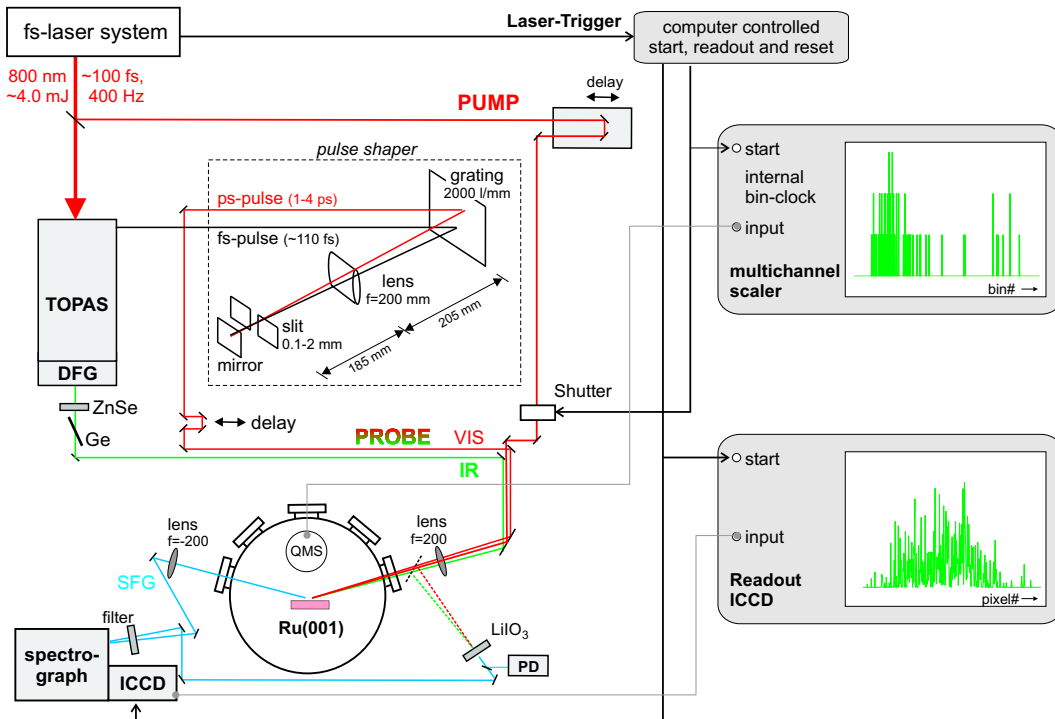

Figure 2.22.: Experimental setup used for the time-resolved investigation of the CO formation on Ru(001) via SFG. The setup consists of the TOPAS and a pulse shaper delivering the two probe pulses, named IR and VIS, and a 800 nm pump pulse which can be delayed in time and switched on and off by a computer controlled shutter. For a distinct series of laser pulses, the TOF and SFG data are recorded. Not shown is the reference beam path for characterizing the pump pulse.

2.5. Performed experiments

of a measurement of the non-resonant SFG background, which is used for normalizing the SFG intensity. Afterwards, the surface is irradiated with a small number (20-50) of pump pulses. The TOF data and the SFG data for those reaction-inducing laser pulse are summed up and read out.

2. Experimental Details

60